

Approximate Riemann Solvers for the Cosmic Ray Magnetohydrodynamical Equations

Yuki Kudoh,^{1*} and Tomoyuki Hanawa²

¹*Department of Physics, Graduate School of Science, Chiba University, 1-33 Yayoi-cho, Inage-ku, Chiba 263-8522, Japan*

²*Center for Frontier Science, Chiba University, 1-33 Yayoi-cho, Inage-ku, Chiba 263-8522, Japan*

Accepted XXX. Received YYY; in original form ZZZ

ABSTRACT

We analyze the cosmic-ray magnetohydrodynamic (CR MHD) equations to improve the numerical simulations. We propose to solve them in the fully conservation form, which is equivalent to the conventional CR MHD equations. In the fully conservation form, the CR energy equation is replaced with the CR “number” conservation, where the CR number density is defined as the three fourths power of the CR energy density. The former contains an extra source term, while latter does not. An approximate Riemann solver is derived from the CR MHD equations in the fully conservation form. Based on the analysis, we propose a numerical scheme of which solutions satisfy the Rankine-Hugoniot relation at any shock. We demonstrate that it reproduces the Riemann solution derived by Pfrommer et al. (2006) for a 1D CR hydrodynamic shock tube problem. We compare the solution with those obtained by solving the CR energy equation. The latter solutions deviate from the Riemann solution seriously, when the CR pressure dominates over the gas pressure in the post-shocked gas. The former solutions converge to the Riemann solution and are of the second order accuracy in space and time. Our numerical examples include an expansion of high pressure sphere in an magnetized medium. Fast and slow shocks are sharply resolved in the example. We also discuss possible extension of the CR MHD equations to evaluate the average CR energy.

Key words: hydrodynamics – MHD – shock waves – methods: numerical – cosmic rays

1 INTRODUCTION

Cosmic rays, referred to CRs in the following, are one of the important constituents in the interstellar and intergalactic media (see e.g. Tielens 2010). The energy density of the CRs is roughly comparable with those of the thermal gas and magnetic field. Thus CRs are expected to play a role in the dynamics and magnetic field structures (see e.g. Longair 1994). Parker (1966; 1967) pointed out that CRs enhance the escape of magnetic flux tubes from the Galactic disc through the Parker instability. They affect also the termination shock of the solar wind (see e.g. Florinski et al. 2013; Potgieter 2013), the galactic winds (see e.g. Bykov 2014), and cosmological structure formation through shocks (see e.g. Pfrommer et al. 2006; Vazza et al. 2012).

The dynamics of CRs are often taken into account by the CR magnetohydrodynamical (MHD) equations. This fluid approximation is justified because CRs are confined by the magnetic field and well scattered by small scale mag-

netic fluctuations (see e.g. Zweibel 2013). CRs are assumed to be an ultrarelativistic gas and hence the pressure is assumed to be one third of the energy density in the CR MHD equations. The CR MHD or CR hydrodynamical (HD) equations have been used for numerical simulations of the interstellar and galactic scales (see e.g. Fahr et al. 2000; Kuwabara et al. 2004; Rasera & Chandran 2008; Yang et al. 2012; Hanasz et al. 2013; Salem & Bryan 2014; Vazza et al. 2015).

The CR MHD equations are similar to the ordinary MHD equations and expressed in the conservation form except for the energy equation for CRs. The energy of CRs is enhanced by compression and consumed by work to the thermal gas. Thus the CR energy equation contains a source term proportional to spatial derivative of either pressure or velocity. This source term has been evaluated separately from the flux in the numerical simulations hitherto. However, this treatment does not guarantee that the numerical solutions satisfy the Rankine-Hugoniot relation for a shock. Although the Rankine-Hugoniot relation and Riemann solutions have been obtained by Pfrommer et al. (2006) for the

* E-mail: kudoyk.aplab@chiba-u.jp (YK)

CR HD equations, the approximate Riemann solvers have not been given in the literature. In other words, the effects of CRs on shocks might not be taken into the simulations properly. Remember that modern HD and MHD simulations rely on the appropriate approximate Riemann solvers to reproduce strong shock waves (see e.g. [Toro 2009](#)). Good approximate Riemann solvers capture strong shocks sharply without artificial oscillations of numerical origin.

In this paper, we rewrite the CR MHD equations into the fully conservation form. One of them describes the conservation of CR *particle number*. Here the CR number density is defined to be the $1/\gamma_{\text{cr}}$ -th power of P_{cr} , where P_{cr} and γ_{cr} denote the pressure and specific heat ratio of CRs, respectively. The Rankine-Hugoniot relation is easily reconstructed from the fully conservation form. We derive the wave properties of the CR MHD equations such as the characteristics, the corresponding right eigenvectors and wave amplitudes. They are used to construct the Roe-type approximate Riemann solver (see e.g. [Toro 2009](#) for the classification of the approximate Riemann solvers). We show that the approximate Riemann solver works well for 1D shock problems and 2D expansion. The former is used for comparison with the exact solution and those obtained with conventional scheme. When the CR pressure is dominant in the post-shocked gas, the solutions obtained with the conventional schemes do not satisfy the Rankine-Hugoniot relation. On the other hand, the Roe-type approximate Riemann solver reproduces the pressure balance mode, a kind of contact discontinuity appearing in the CR MHD equation, as well as the shock.

This paper is organized as follows. We derive the fully conservation form of the CR MHD equations in Section 2.1. The Rankine-Hugoniot relation is derived in Section 2.2. The approximate Riemann solution is given in Section 2.3. Numerical tests are shown in Section 3. Section 3.1 is devoted to the 1D CR HD shock tube problem. Section 3.2 is devoted to the linear wave test, while Section 3.3 to the advection of the pressure balance mode. Section 3.4 is devoted to the 1D CR MHD shock tube problem, while Section 3.5 is to 2D CR MHD problem. We discuss the shock tube problems solved by [Pfrommer et al. \(2006\)](#) and [Dubois & Commerçon \(2016\)](#) in Section 4. We also discuss possible extension of the CR MHD equations to evaluate the average CR particle energy before conclusion. This paper is based on our earlier work, [Kudoh & Hanawa \(2016\)](#), but improved to achieve the second order accuracy.

2 SYSTEM OF CR MHD EQUATION

First we introduce the CR MHD equations according to [Berezinskii et al. \(1990\)](#) in which the fluid approximation is applied to CRs. The equation of continuity,

$$\frac{\partial \rho}{\partial t} + \nabla \cdot (\rho \mathbf{v}) = 0, \quad (1)$$

and the induction equation,

$$\frac{\partial \mathbf{B}}{\partial t} - \nabla \times (\mathbf{v} \times \mathbf{B}) = 0, \quad (2)$$

are the same as those of the ordinary MHD equations. Here the symbols, ρ , \mathbf{v} , and \mathbf{B} denote the density, velocity, and

magnetic field, respectively. The CR pressure, P_{cr} , is taken into account in the equation of motion,

$$\frac{\partial}{\partial t} (\rho \mathbf{v}) + \nabla \cdot \left[\rho \mathbf{v} \mathbf{v} + \left(P_{\text{g}} + P_{\text{cr}} + \frac{|\mathbf{B}|^2}{2} \right) \mathbf{I} - \mathbf{B} \mathbf{B} \right] = 0, \quad (3)$$

where P_{g} and \mathbf{I} denote the gas pressure and the unit tensor, respectively. Accordingly the equation of energy conservation is altered into

$$\frac{\partial}{\partial t} (E) + \nabla \cdot [(E + P_{\text{g}}) \mathbf{v} - (\mathbf{v} \times \mathbf{B}) \times \mathbf{B}] = -\mathbf{v} \cdot \nabla P_{\text{cr}}, \quad (4)$$

$$E = \frac{\rho}{2} |\mathbf{v}|^2 + \frac{P_{\text{g}}}{\gamma_{\text{g}} - 1} + \frac{|\mathbf{B}|^2}{2}, \quad (5)$$

where γ_{g} , denotes the specific heat ratio of the gas. The gas is assumed to be an ideal gas with $\gamma_{\text{g}} = 5/3$ throughout this paper except when otherwise noted.

CRs are approximated to be an ideal gas having the constant specific heat ratio, $\gamma_{\text{cr}} = 4/3$. Then the CR energy density, E_{cr} , is evaluated to be

$$E_{\text{cr}} = \frac{P_{\text{cr}}}{\gamma_{\text{cr}} - 1}. \quad (6)$$

The CR energy equation is expressed as

$$\frac{\partial}{\partial t} (E_{\text{cr}}) + \nabla \cdot [(E_{\text{cr}} + P_{\text{cr}}) \mathbf{v}] = \mathbf{v} \cdot \nabla P_{\text{cr}} - \nabla \cdot \mathbf{F}_{\text{diff}}, \quad (7)$$

$$\mathbf{F}_{\text{diff}} = -\kappa_{\perp} \nabla E_{\text{cr}} - (\kappa_{\parallel} - \kappa_{\perp}) \frac{(\mathbf{B} \cdot \nabla E_{\text{cr}}) \mathbf{B}}{|\mathbf{B}|^2}, \quad (8)$$

where advection, the work to accelerate the gas, and diffusion are taken into account. The symbols, κ_{\parallel} and κ_{\perp} , denote the diffusion coefficients in the directions parallel and perpendicular to the magnetic field, respectively.

In the following we analyse the case of no diffusion ($\kappa_{\parallel} = \kappa_{\perp} = 0$). As shown later, the CR MHD equations are hyperbolic and the characteristic speeds are independent of the wavelength in this case. Remember that the diffusion is often taken account separately in numerical simulations by means of the operator splitting. In other words, the diffusion is not taken into account in the construction of approximate Riemann solutions. Thus our approach to the CR MHD equation is orthodox.

2.1 Fully conservation Form

Next we rewrite the CR MHD equations in the fully conservation form. While equations (1)-(3) are written in the conservation form, equations (4) and (7) are not. The sum of equations (4) and (7) gives us the equation of the total energy conservation,

$$\frac{\partial}{\partial t} (E + E_{\text{cr}}) + \nabla \cdot [(E + E_{\text{cr}} + P_{\text{g}} + P_{\text{cr}}) \mathbf{v} - (\mathbf{v} \times \mathbf{B}) \times \mathbf{B}] = 0. \quad (9)$$

Thus the CR MHD equations are expressed in the fully conservation form if equation (7) is converted into the conservation form.

For later convenience we introduce the CR number density defined as

$$\rho_{\text{cr}} \equiv P_{\text{cr}}^{1/\gamma_{\text{cr}}}, \quad (10)$$

which is equivalent to equation (3.6) in Pfrommer et al. (2006). Equation (10) implies that CRs are approximated by a polytrope gas. Then equation (7) is rewritten in the conservation form,

$$\frac{\partial}{\partial t} \rho_{\text{cr}} + \nabla \cdot (\rho_{\text{cr}} \mathbf{v}) = 0, \quad (11)$$

when $\kappa_{\parallel} = \kappa_{\perp} = 0$.

Note the similarity between equations (1) and (11). From these equations we can derive

$$\frac{d}{dt} \left(\frac{\rho_{\text{cr}}}{\rho} \right) = 0. \quad (12)$$

For later convenience we introduce the concentration of CRs defined as

$$\chi = \frac{\rho_{\text{cr}}}{\rho}. \quad (13)$$

When all the variables depend only on t and x (1D), the CR MHD equations are expressed in the vector form,

$$\frac{\partial \mathbf{U}}{\partial t} + \frac{\partial \mathbf{F}}{\partial x} = 0, \quad (14)$$

$$\mathbf{U} = \begin{bmatrix} \rho \\ \rho v_x \\ \rho v_y \\ \rho v_z \\ B_x \\ B_y \\ B_z \\ \rho H - P_{\text{T}} + \frac{|\mathbf{B}|^2}{2} \\ \rho \chi \end{bmatrix}, \quad (15)$$

$$\mathbf{F} = \begin{bmatrix} \rho v_x \\ \rho v_x^2 + P_{\text{T}} + \frac{|\mathbf{B}|^2}{2} - B_x^2 \\ \rho v_x v_y - B_x B_y \\ \rho v_x v_z - B_x B_z \\ 0 \\ v_x B_y - v_y B_x \\ v_x B_z - v_z B_x \\ \rho H v_x + |\mathbf{B}|^2 v_x - (\mathbf{v} \cdot \mathbf{B}) B_x \\ \rho \chi v_x \end{bmatrix}, \quad (16)$$

$$H = \frac{v^2}{2} + \frac{\gamma_{\text{g}}}{\gamma_{\text{g}} - 1} \frac{P_{\text{g}}}{\rho} + \frac{\gamma_{\text{cr}}}{\gamma_{\text{cr}} - 1} \frac{P_{\text{cr}}}{\rho}, \quad (17)$$

$$P_{\text{T}} = P_{\text{g}} + P_{\text{cr}}. \quad (18)$$

where \mathbf{U} and \mathbf{F} denote the state and flux vectors, respectively. We use this vector form to derive the Rankine-Hugniot relation and Riemann solution.

2.2 Rankine-Hugniot relation

In this subsection we derive the Rankine-Hugniot relation, i.e., the jump condition at a shock front, using the CR MHD equations in the conservation form, equations (14), (15) and (16). For simplicity we restrict ourselves to a stationary plane shock. In other words, we observe a small area around a shock wave in the comoving frame. Furthermore, the wave

front is assumed to be normal to the x -direction in the Cartesian coordinates. Since the temporal change vanishes, then the flux, \mathbf{F} , should be continuous across the shock front,

$$[\rho v_x] = 0, \quad (19)$$

$$\left[\rho v_x^2 + P_{\text{T}} + \frac{B_y^2 + B_z^2 - B_x^2}{2} \right] = 0, \quad (20)$$

$$[\rho v_x v_y - B_x B_y] = 0, \quad (21)$$

$$[\rho v_x v_z - B_x B_z] = 0, \quad (22)$$

$$[v_x B_y - v_y B_x] = 0, \quad (23)$$

$$[v_x B_z - v_z B_x] = 0, \quad (24)$$

$$[\rho H v_x + (B_y^2 + B_z^2) v_x - (v_y B_y + v_z B_z) B_x] = 0, \quad (25)$$

$$[\rho \chi v_x] = 0, \quad (26)$$

where the symbol $[\cdot]$ denotes the jump across the discontinuity. Here, the subscripts, x , y , and z denote the x -, y -, and z -components, respectively. These conditions are the same as those obtained by Pfrommer et al. (2006) and almost the same as those for the MHD equations except for equation (26): equations (20) and (25) are modified to include P_{cr} and E_{cr} . Equation (26) denotes the continuity of the CR number flux. Combining equations (19) through (26) we obtain

$$\frac{\rho_{\text{cr}}}{\rho} = \chi = \text{const.}, \quad (27)$$

across the shock. This means that the CR pressure changes only through the gas compression or expansion.

2.3 Elementary Wave Solutions of the Riemann Problem

First we examine the CR HD equations, since inclusion of CRs changes the equation of state but does not alter the induction equation. Furthermore we consider a 1D flow in which the y - and z -components vanish. Then the state and flux vectors are expressed as

$$\mathbf{U} = \begin{bmatrix} \rho \\ \rho v_x \\ \rho H - P_{\text{T}} \\ \rho \chi \end{bmatrix}, \quad (28)$$

$$\mathbf{F} = \begin{bmatrix} \rho v_x \\ \rho v_x^2 + P_{\text{T}} \\ \rho H v_x \\ \rho \chi v_x \end{bmatrix}. \quad (29)$$

As shown later, inclusion of the tangential velocity and magnetic field are straight forward.

CRs increase the total pressure and hence the sound speed. The total pressure is expressed as

$$P_{\text{T}} = P_{\text{g}} + (\chi \rho)^{\gamma_{\text{cr}}}, \quad (30)$$

as shown in the previous subsection. Then the adiabatic sound speed is evaluated to be

$$a = \left[\left(\frac{\partial P_{\text{g}}}{\partial \rho} \right)_s + \left(\frac{\partial P_{\text{cr}}}{\partial \rho} \right)_\chi \right]^{1/2} = \left(\frac{\gamma_{\text{g}} P_{\text{g}} + \gamma_{\text{cr}} P_{\text{cr}}}{\rho} \right)^{1/2}, \quad (31)$$

$$s = \ln P_{\text{g}} - \gamma_{\text{g}} \ln \rho, \quad (32)$$

where s denotes the entropy, since $d\chi/dt = 0$ (equation 12). Note that the entropy is constant

$$\frac{ds}{dt} = 0, \quad (33)$$

for a given gas element except for increase at a shock.

The characteristics of the CR HD equations are the eigenvalues of the Jacobian matrix,

$$\mathbf{A} \equiv \partial \mathbf{F} / \partial \mathbf{U}. \quad (34)$$

We obtain four characteristics,

$$\lambda_{1,4} = v_x \pm a, \quad (35)$$

$$\lambda_{2,3} = v_x, \quad (36)$$

after some algebra. The former denotes the sound wave while the latter does advection. The additional advection mode corresponds to conservation of the CR concentration (equation 27) and hence to the pressure balance mode. The others are the same as those in the ordinary HD equations except for the change in the sound speed.

The spatial derivative of \mathbf{U} and \mathbf{F} are decomposed into waves. They are expressed as

$$\frac{\partial \mathbf{U}}{\partial x} = \sum_{i=1}^4 w_i \mathbf{r}_i, \quad (37)$$

$$\frac{\partial \mathbf{F}}{\partial x} = \sum_{i=1}^4 \lambda_i w_i \mathbf{r}_i, \quad (38)$$

where

$$w_{1,4} = \frac{1}{2a^2} \left(\frac{\partial P_T}{\partial x} \pm \rho a \frac{\partial v_x}{\partial x} \right), \quad (39)$$

$$w_2 = \frac{\partial \rho}{\partial x} - \frac{1}{a^2} \frac{\partial P_T}{\partial x} = -\frac{P_g}{a^2} \frac{\partial s}{\partial x} - \frac{\rho \chi^{-1}}{a^2} \left(\frac{\partial P_{cr}}{\partial \rho} \right)_\chi \frac{\partial \chi}{\partial x}, \quad (40)$$

$$w_3 = \frac{\partial \rho_{cr}}{\partial x} - \chi \frac{\partial \rho}{\partial x} = \rho \frac{\partial \chi}{\partial x}, \quad (41)$$

$$\mathbf{r}_{1,4} = \begin{bmatrix} 1 \\ v_x \pm a \\ H \pm a v_x \\ \chi \end{bmatrix}, \quad \mathbf{r}_2 = \begin{bmatrix} 1 \\ v_x \\ \frac{v_x^2}{2} + \chi \zeta \\ \chi \end{bmatrix}, \quad \mathbf{r}_3 = \begin{bmatrix} 0 \\ 0 \\ \zeta \\ 1 \end{bmatrix}, \quad (42)$$

$$\zeta = \frac{\gamma_g - \gamma_{cr}}{(\gamma_g - 1)(\gamma_{cr} - 1)} \frac{dP_{cr}}{d\rho_{cr}}. \quad (43)$$

Here the symbol, w_i , denotes the amplitude of the i -th wave. Inclusion of CRs introduces a new Riemann invariant, χ , and change the other Riemann invariants only slightly. The symbol, ζ , denotes the change in the energy density due to the pressure balance mode (Webb et al. 1995). The energy density depends on the proportion of P_{cr} for a given P_T .

Equations (37) through (42) are used to construct the Roe (1981) type approximate Riemann solvers for numerical simulations. Further details are given in Appendix A.

Also the exact Riemann solutions are derived from equations (37) through (42). Here the Riemann solution

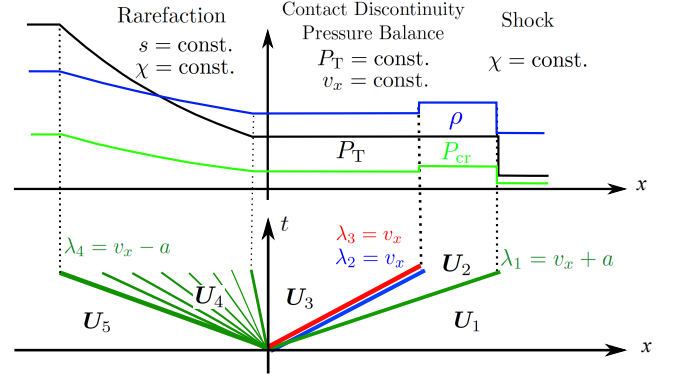


Figure 1. Illustration of the Riemann solution for a CR HD shock tube problem. The density, total pressure and CR pressure are shown as a function of x in the upper half. The lower half denotes the characteristics.

means that the solution of equation (14), when the initial condition is expressed as

$$\mathbf{U} = \begin{cases} \mathbf{U}_L & x < 0 \\ \mathbf{U}_R & x \geq 0 \end{cases}, \quad (44)$$

at $t = 0$. The Riemann solution is obtained from the conditions,

$$w_i = 0, \quad (45)$$

except at discontinuities. However, the algorithm to obtain the complete solution is lengthy even for the ordinary HD equations, as shown in Toro (2009). Pfrommer et al. (2006) showed the Riemann solution for the case in which a shock propagates rightward and a rarefaction wave propagates leftward.

Fig. 1 illustrates an example of the Riemann solution. In this solution a shock wave travels at the speed, λ_1 , while the contact discontinuity and the pressure balance mode at $\lambda_2 (= \lambda_3)$. The rarefaction wave has the head and tail. The state vector is uniform in each region separated by the characteristics except between the head and tail of the rarefaction wave. We refer to regions 1 through 5 from right to left in the figure. The Rankine-Hugoniot relation is applied to the jump between regions 1 and 2. The total pressure and velocity are continuous at the boundary between regions 2 and 3, while the entropy and CR concentration are not. The velocity gradient in region 4 is obtained from

$$\frac{dv_x}{dx} = \frac{1}{\rho a} \frac{dP_T}{dx}, \quad (46)$$

$s = \text{const.}$, $\chi = \text{const.}$, and $\lambda_4 = v_x - a$. The state vector remains at the initial value, $\mathbf{U}_1 = \mathbf{U}_R$ and $\mathbf{U}_5 = \mathbf{U}_L$, in regions 1 and 5. In short the Riemann solution changes only quantitatively by inclusion of CRs.

Next we consider the Riemann solution of the CR MHD equations. The ordinary MHD equations have 7 characteristics: three pairs of the fast, slow, and Alfvén waves in addition to the entropy wave. CRs add the pressure balance mode and modify the phase speeds of the fast and slow waves through the change in the sound speed. After some algebra, we have found the following formulae for λ_i , w_i , and \mathbf{r}_i for the CR MHD equations using the formulation given by

Ryu & Jones (1995) for the ordinary MHD equations.

$$\lambda_{1,8} = v_x \pm c_f, \quad (47)$$

$$\lambda_{3,6} = v_x \pm c_s, \quad (48)$$

$$\lambda_{4,5} = v_x, \quad \lambda_{2,7} = v_x \pm v_{Ax}, \quad (49)$$

$$\begin{aligned} w_1 + w_8 &= \frac{\alpha_f}{c_f^2} \left(\frac{\partial P_T}{\partial x} + B_y \frac{\partial B_y}{\partial x} + B_z \frac{\partial B_z}{\partial x} \right) \\ &+ \left[\frac{\alpha_s \sqrt{\rho}}{a^2 c_f} \left\{ (\gamma_g - 1) c_s^2 - (\gamma_g - 2) a^2 \right\} \right. \\ &\quad \left. + \frac{\alpha_f}{c_f^2} (\gamma_g - 2) \sqrt{B_y^2 + B_z^2} \right] \left(\beta_y \frac{\partial B_y}{\partial x} + \beta_z \frac{\partial B_z}{\partial x} \right), \end{aligned} \quad (50)$$

$$w_1 - w_8 = \frac{\alpha_f}{c_f} \rho \frac{\partial v_x}{\partial x} - \frac{\alpha_s c_s}{c_f a} \rho \operatorname{sgn}(B_x) \left(\beta_y \frac{\partial B_y}{\partial x} + \beta_z \frac{\partial B_z}{\partial x} \right), \quad (51)$$

$$\begin{aligned} w_3 + w_6 &= \frac{\alpha_s}{a^2} \left(\frac{\partial P_T}{\partial x} + B_y \frac{\partial B_y}{\partial x} + B_z \frac{\partial B_z}{\partial x} \right) \\ &+ \left[\frac{\alpha_f \sqrt{\rho}}{a^2 c_f} \left\{ (\gamma_g - 2) a^2 - (\gamma_g - 1) c_f^2 \right\} \right. \\ &\quad \left. + \frac{\alpha_s}{a^2} (\gamma_g - 2) \sqrt{B_y^2 + B_z^2} \right] \left(\beta_y \frac{\partial B_y}{\partial x} + \beta_z \frac{\partial B_z}{\partial x} \right), \end{aligned} \quad (52)$$

$$w_3 - w_6 = \frac{\alpha_s v_{Ax}}{c_f a} \rho \frac{\partial v_x}{\partial x} + \frac{\alpha_f}{a} \rho \operatorname{sgn}(B_x) \left(\beta_y \frac{\partial B_y}{\partial x} + \beta_z \frac{\partial B_z}{\partial x} \right), \quad (53)$$

$$w_4 = \frac{\partial \rho}{\partial x} - \alpha_f (w_1 + w_8) - \alpha_s (w_3 + w_6), \quad (54)$$

$$w_5 = \rho \frac{\partial \chi}{\partial x}, \quad (55)$$

$$\begin{aligned} w_{2,7} &= \frac{1}{2} \left[\mp \rho \left(\beta_z \frac{\partial v_y}{\partial x} - \beta_y \frac{\partial v_z}{\partial x} \right) \operatorname{sgn}(B_x) \right. \\ &\quad \left. + \sqrt{\rho} \left(\beta_z \frac{\partial B_y}{\partial x} - \beta_y \frac{\partial B_z}{\partial x} \right) \right], \end{aligned} \quad (56)$$

$$\mathbf{r}_{1,8} = \begin{bmatrix} \alpha_f \\ \alpha_f (v_x \pm c_f) \\ \alpha_f v_y \mp \alpha_s \beta_y v_{Ax} \operatorname{sgn}(B_x) \\ \alpha_f v_z \mp \alpha_s \beta_z v_{Ax} \operatorname{sgn}(B_x) \\ \frac{\alpha_s \beta_y c_f}{\sqrt{\rho}} \\ \frac{\alpha_s \beta_z c_f}{\sqrt{\rho}} \\ R_{1,8} \\ \alpha_f \chi \end{bmatrix}, \quad (57)$$

$$\mathbf{r}_{3,6} = \begin{bmatrix} \alpha_s \\ \alpha_s (v_x \pm c_s) \\ \alpha_s v_y \pm \alpha_f \beta_y a \operatorname{sgn}(B_x) \\ \alpha_s v_z \mp \alpha_f \beta_z a \operatorname{sgn}(B_x) \\ -\frac{\alpha_f \beta_y a^2}{c_f \sqrt{\rho}} \\ -\frac{\alpha_f \beta_z a^2}{c_f \sqrt{\rho}} \\ R_{3,6} \\ \alpha_s \chi \end{bmatrix}, \quad (58)$$

$$\mathbf{r}_{2,7} = \begin{bmatrix} 0 \\ 0 \\ \mp \beta_z \operatorname{sgn}(B_x) \\ \pm \beta_y \operatorname{sgn}(B_x) \\ \beta_z / \sqrt{\rho} \\ -\beta_y / \sqrt{\rho} \\ R_{2,7} \\ 0 \end{bmatrix}, \quad \mathbf{r}_4 = \begin{bmatrix} 1 \\ v_x \\ v_y \\ v_z \\ 0 \\ 0 \\ R_4 \\ \chi \end{bmatrix}, \quad \mathbf{r}_5 = \begin{bmatrix} 0 \\ 0 \\ 0 \\ 0 \\ 0 \\ 0 \\ \zeta \\ 1 \end{bmatrix}, \quad (59)$$

where,

$$R_4 = \frac{|v|^2}{2} + \chi \zeta, \quad R_{2,7} = \mp (\beta_z v_y - \beta_y v_z) \operatorname{sgn}(B_x), \quad (60)$$

$$\begin{aligned} R_{1,8} &= \alpha_f \left\{ R_4 \pm c_f v_x + \frac{c_f^2}{\gamma_g - 1} + \frac{\gamma_g - 2}{\gamma_g - 1} (c_f^2 - a^2) \right\} \\ &\quad \mp \alpha_s v_{Ax} \operatorname{sgn}(B_x) (\beta_y v_y + \beta_z v_z), \end{aligned} \quad (61)$$

$$\begin{aligned} R_{3,6} &= \alpha_s \left\{ R_4 \pm c_s v_x + \frac{c_s^2}{\gamma_g - 1} + \frac{\gamma_g - 2}{\gamma_g - 1} (c_s^2 - a^2) \right\} \\ &\quad \pm \alpha_f a \operatorname{sgn}(B_x) (\beta_y v_y + \beta_z v_z), \end{aligned} \quad (62)$$

$$v_{Ax}^2 = \frac{B_x^2}{\rho}, \quad a_*^2 = a^2 + \frac{B_x^2 + B_y^2 + B_z^2}{\rho}, \quad (63)$$

$$c_{f,s}^2 = \frac{1}{2} \left(a_*^2 \pm \sqrt{a_*^4 - 4a^2 v_{Ax}^2} \right), \quad (64)$$

$$\alpha_f = \frac{\sqrt{c_f^2 - v_{Ax}^2}}{\sqrt{c_f^2 - c_s^2}}, \quad \alpha_s = \frac{\sqrt{c_f^2 - a^2}}{\sqrt{c_f^2 - c_s^2}}, \quad \alpha_f^2 + \frac{v_{Ax}^2}{c_f^2} \alpha_s^2 = 1, \quad (65)$$

$$\beta_y = \frac{B_y}{\sqrt{B_y^2 + B_z^2}}, \quad \beta_z = \frac{B_z}{\sqrt{B_y^2 + B_z^2}}, \quad \beta_y^2 + \beta_z^2 = 1. \quad (66)$$

The above formulae are also used to construct the Roe

Table 1. The initial state in the CR HD shock tube problem.

	ρ	v_x	P_g	P_{cr}
Left ($x < 0$)	1.0	0.0	2.0	1.0
Right ($x \geq 0$)	0.2	0.0	0.02	0.1

type approximate Riemann solutions. The Roe average is given in Appendix A. It is difficult to obtain the exact CR MHD Riemann solution although it may not be impossible.

3 NUMERICAL TESTS

We examine whether we can reproduce the Riemann solution given in the previous section in numerical simulations. CR MHD simulations thus far have solved equation (7) instead of equation (11). We show that a solution of equation (7) does not satisfy the Rankine-Hugoniot relation for a 1D CR HD shock tube problem, while equation (11) does. We also demonstrate equation (11) provides appropriate solutions for 1D CR MHD shock tube problem and 2D CR MHD expansion problem.

We use the explicit scheme of the second order accuracy in space and time except when otherwise noted. The second order accuracy in space is achieved by the Monotone Upstream-Centered Schemes for Conservation Laws (MUSCL) with characteristics (van Leer 1979; and see e.g. Toro 2009). When we solve equation (7), we interpolate the primitive variables, ρ , P_g , P_{cr} , v_x , v_y , v_z , B_x , B_y , and B_z . When we solve the fully conservative form of the CR MHD equations, we interpolate the wave amplitudes, w_i , instead of the primitive variables. The interpolated variables are chosen to achieve the second order accuracy in solving the pressure balance mode. The second order accuracy in time is achieved by the two stage Runge-Kutta method. All the test problems are solved on a uniform cell width and with a constant time step.

3.1 1D CR HD shock tube problem

In this subsection, we solve a CR HD shock tube problem with four different schemes. Two of them solve equation (11) while the others two not. The initial state is summarized in Table 1. The left-hand side has a higher pressure and hence the shock wave runs rightward with the speed, 2.369. The head of the rarefaction wave runs leftward with the speed, -2.160. The spatial resolution is $\Delta x = 1/128$ and the time step is fixed at $\Delta t = 2.0 \times 10^{-3}$. Accordingly the Courant-Friedrich-Lewy (CFL) number is 0.780 in the simulations shown below.

First we solve the CR HD equations in the fully conservation form, in which the state and flux vectors are given by equations (28) and (29), with the Roe-type approximate Riemann solver. The solution at $t = 0.1$ is shown in Fig. 2. The top panels show the density, velocity, and entropy from left to right, respectively. The bottom left-hand panel shows P_g by the red curve and P_T by the black curve. The bottom central panel denotes P_{cr} by the yellow green while the bottom right-hand panel does CR concentration (χ) by the green. The plus symbols denote the data points. The black

curves without symbols denote the Riemann solution, while the dashed lines do the initial state.

The shock front and rarefaction wave are reproduced well in Fig. 2. The contact discontinuity ($x = 0.156$) is also reproduced well. Note that CR concentration, χ , is constant across the shock and changes at the contact discontinuity.

Fig. 3 compares this solution with three other solutions obtained with different schemes. Each panel shows the enlargement around the interval between the shock front and contact discontinuity where the differences are large. The top left and right panels denote P_g and s at $t = 0.1$, respectively, while the bottom left and right ones P_{cr} and χ , respectively. The red curves denote the solution shown in Fig. 2.

The green curves denote the solution obtained with the Harten-Lax-van Leer (HLL) scheme (see e.g. Toro 2009) applied to the fully conservation form of the CR HD equations. The maximum and minimum characteristics are evaluated to be $v_x \pm a$ in the HLL scheme. It provides a good approximation around the shock while the deviation from the Riemann solution is large around the contact discontinuity.

The blue curves denote the solution of equation (7). The source term, the right hand side, is evaluated by the central difference. The other equations are solved with the HLL scheme. This scheme is named vdP scheme after the source term. Similar schemes are employed in Kuwabara et al. (2004). This solution is different from the Riemann solution between the shock front and contact discontinuity. The gas pressure is lower and cosmic ray pressure is higher.

The purple curves denote solution obtained by solving

$$\frac{\partial}{\partial t} (E_{cr}) + \nabla \cdot (E_{cr} \mathbf{v}) = -P_{cr} \nabla \cdot \mathbf{v}, \quad (67)$$

which is derived from equation (7). The right hand side is evaluated by the central difference and the other equations are solved with the HLL scheme, which we call Pdv scheme in the following. Similar schemes are employed in Hanasz & Lesch (2003), Yang et al. (2012), and Dubois & Commerçon (2016). This solution is also quite different from the Riemann solution between the shock front and contact discontinuity.

When we solve equation (7) instead of equation (11), we cannot reproduce the Riemann solution. The difference comes in part from the MUSCL approach. Fig. 3 is the same as Fig. 4 except that the solution is of the first order accuracy in space and time. All the solutions of the first order accuracy are very diffusive around the contact discontinuity as expected.

The Roe-type approximate Riemann solver is, however, still close to the Riemann solution. The HLL scheme produces a hump in P_g and a dump in P_{cr} around the contact discontinuity in the first order solution. The hump and dump are much smaller in the second order solution. This implies that they are due to numerical diffusion. We will discuss the origin of the hump and bump in Section 3.3. The numerical solutions are still acceptable in the first order accuracy when we solve the fully conservation form.

The solution obtained with the vdP scheme shows serious enhancement in χ at the shock front. The entropy has a dip at the shock front and the shock propagation speed is underestimated. The CR pressure is overestimated while the gas pressure is underestimated. The vdP scheme dif-

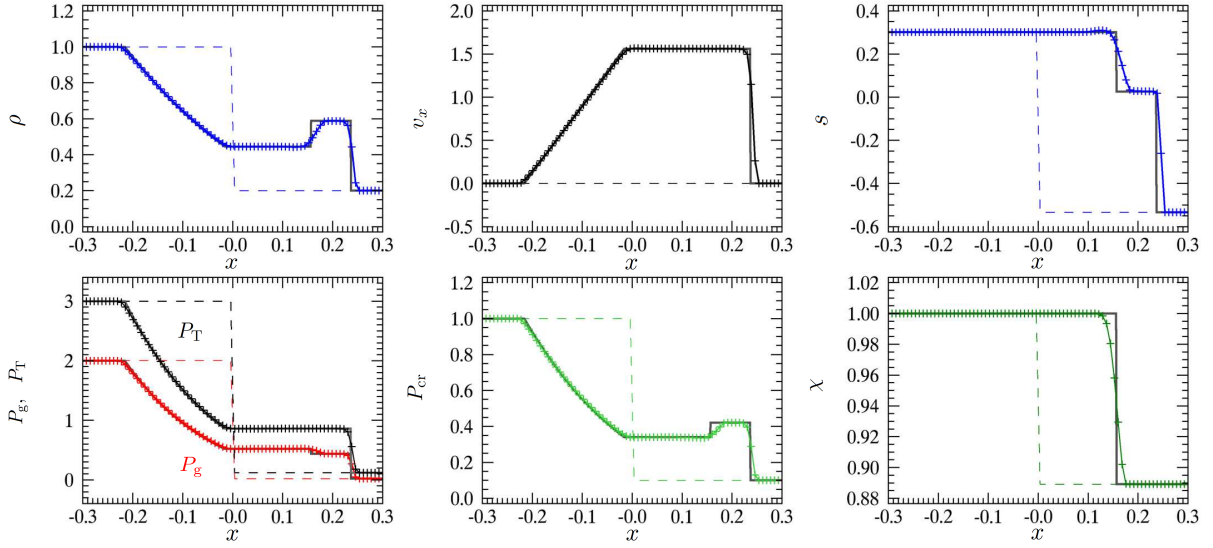


Figure 2. The numerical solution of the CR HD shock tube problem compared with the analytic Riemann solution (thin black solid) and the initial state (dashed). The numerical solution (symbols) is of the second order accuracy and obtained with the Roe-type Riemann solver. Top: ρ , v_x and s from left to right. Bottom: P_g , P_T , P_{cr} and χ from left to right.

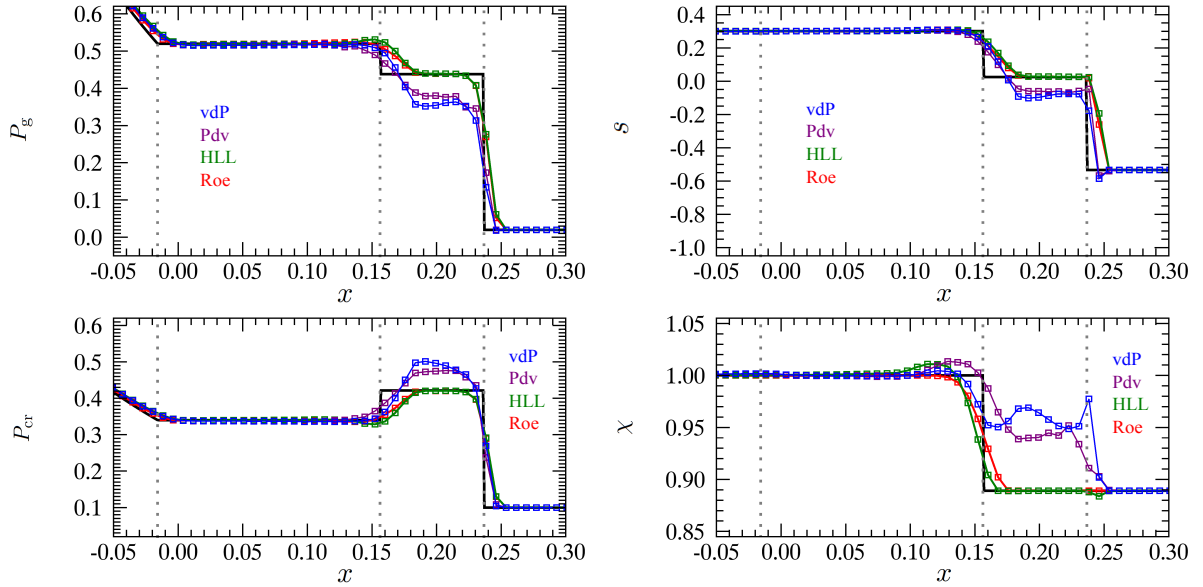


Figure 3. Comparison of the numerical solutions with the 2nd order accuracy in the CR HD shock tube problem. The green and red curves denote the solutions obtained with the CR HD equations in the conservation form while the blue and purple curves do those obtained with the equations with source terms. Top: the gas pressure (left) and the entropy (right). Bottom: the CR pressure (left) and the CR concentration (right). See the main text for further details.

fuses the pressure balance mode seriously. This is because the source term diverges at the pressure balance mode in the vdP scheme.

Also the Pdv scheme overestimates the CR pressure and underestimates the gas pressure. However the difference from the Riemann solution is smaller in the solution of the first order accuracy than in that of the second order accuracy. The solution of the second order accuracy depends a little on the choice of variables to be interpolated. How-

ever, we could not find any good solution of the second order accuracy when we solve equation (11). The source term is extremely large and formally diverges at the shock front in the Pdv scheme. Accordingly the Rankine-Hugoniot relation is not satisfied. The numerical solution around the shock is not improved by the MUSCL approach.

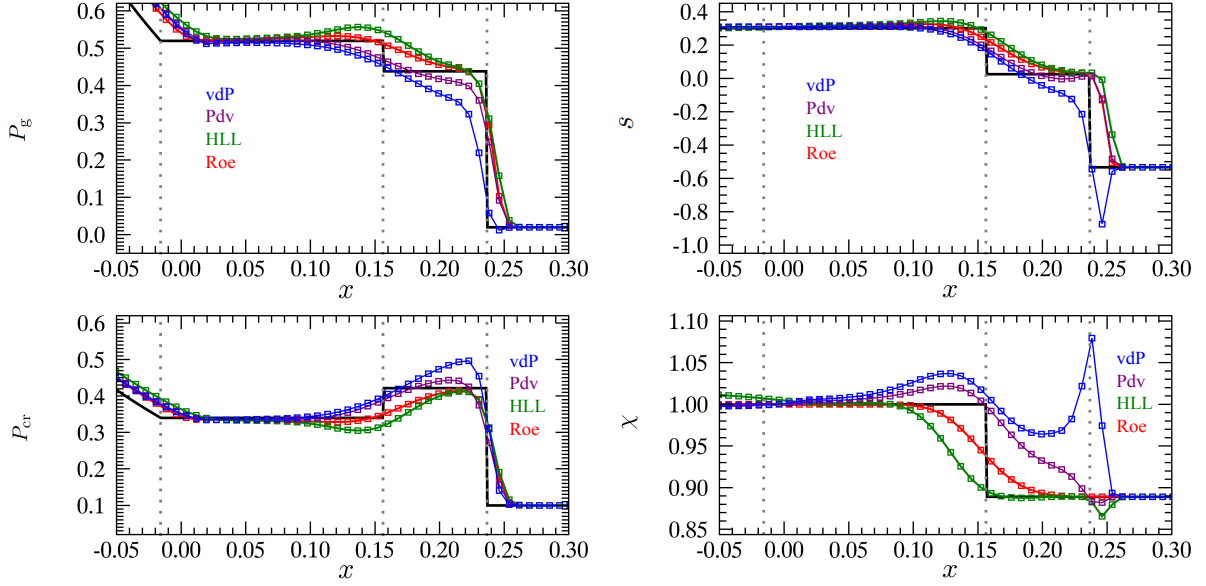


Figure 4. The same as Fig. 3 but for the numerical solution of the 1st order accuracy.

3.2 Linear Wave Test

We examine the propagation of 1D plane waves of a small amplitude in order to confirm the accuracy of our scheme. In the following we follow a sound wave, entropy wave, and the pressure balance mode. The initial state at $t = 0$ is taken to be

$$\rho = \rho_0 + \varepsilon_\rho \cos\left(\frac{2\pi x}{\lambda}\right), \quad (68)$$

$$P_g = P_{g,0} + \varepsilon_g \cos\left(\frac{2\pi x}{\lambda}\right), \quad (69)$$

$$P_{cr} = P_{cr,0} + \varepsilon_{cr} \cos\left(\frac{2\pi x}{\lambda}\right), \quad (70)$$

$$v_x = v_{x,0} + \varepsilon_v \cos\left(\frac{2\pi x}{\lambda}\right), \quad (71)$$

where λ denotes the wavelength. The other parameters are summarized in Table 2. Note that the sound speed is set to be $a = 1.0$ in all the models. The time step is taken to be $\Delta t = 0.5\Delta x/a$. The size of the computation box is the same as the wavelength and the periodic boundary condition is applied.

We measure the numerical error at the epoch at which the wave propagates by a wavelength, i.e., $t = \lambda/a$ for the sound wave and $t = \lambda/v_0$ for the other waves. We use the L1 norm defined as

$$\delta q(t) = \frac{1}{N\varepsilon_q} \sum_j |q_{\text{numerical}}(x_j, t) - q_{\text{exact}}(x_j, t)|, \quad (72)$$

where the symbol, q , denotes a physical quantity. The numerical and exact solutions are denoted by $q_{\text{numerical}}(x_j, t)$ and $q_{\text{exact}}(x_j, t)$, respectively. The symbols, N and ε_q , denote

Table 2. The initial states in the linear wave propagation tests

	Sound	Entropy	Pressure balance
ρ_0	1.0	1.0	1.0
$P_{g,0}$	1/3	1/3	1/3
$P_{cr,0}$	1/3	1/3	1/3
$v_{x,0}$	0.0	0.5	0.5
ε_ρ (10^{-6})	1.0	1.0	0.0
ε_g (10^{-6})	$\gamma_g/3$	0.0	-1.0
ε_{cr} (10^{-6})	$\gamma_{cr}/3$	0.0	1.0
ε_v (10^{-6})	1.0	0.0	0.0

the number of cell in a wavelength and the wave amplitude in the variable, q .

Fig. 5 denotes $\delta\rho(\lambda/a)$ in the sound wave as a function of $\Delta x/\lambda \equiv 1/N$ by the green crosses and circles, the former and latter of which are obtained with the first- and second-order schemes, respectively. The red crosses and circles are the same as the green ones but for $\delta P_{cr}(\lambda/v_{x,0})$ in the pressure balance mode. We denote the error in the entropy mode, $\delta\rho(\lambda/v_{x,0})/2$, by the blue crosses and circles. The factor, $1/2$, is introduced to avoid the overlap with the red symbols. Our second order schemes solve all these hydrodynamical waves with the second order accuracy in space.

Also the Pdv and vdP scheme provide the solutions of the second order accuracy for the test problems examined in this subsection. As far as the wave amplitude is small, all the schemes provide nearly the same results as expected.

3.3 Advection of the Pressure Balance Mode

The pressure balance mode produces some unphysical features such as spurious enhancement in the gas pressure and

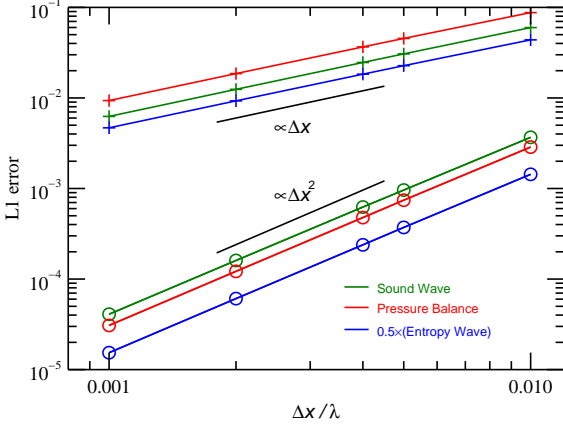


Figure 5. The L1 norm of the numerical error is shown as a function of the cell width in unit of the wavelength. The crosses denote the errors in the solution of the first order accuracy, while the circles denote those of the second order accuracy. The green, blue and red symbols are for the sound wave, pressure balance mode, and the entropy wave, respectively.

dent in the CR pressure as shown in Fig. 4. It also emits spurious sound waves as shown later in this subsection. We identify the origin and provide a remedy. The initial state of the test problem is summarized in Table 3. The velocity should remain constant in this problem since the total pressure has the same value in the both sides. The cell width and time step are taken to be $\Delta x = 0.1$ and $\Delta t = 0.025$, respectively. Accordingly the CFL number is 0.585 in the simulations shown below.

The spurious sound wave appears from the beginning irrespectively of the numerical scheme applied. Fig. 6 shows the solutions at the first three time steps, i.e., at $t = 0.000$, 0.025, and 0.050 from top to bottom. The left-hand and central panels show P_g and P_T , respectively, while the right-hand panels show v_x . The green and red curves with the symbols denote the solutions obtained with the HLL scheme and the Roe-type Riemann solver, respectively, while the black lines denote the exact solution. The accuracy of these solutions is the first order in space and in time. The total pressure is enhanced at the second time step ($t = 0.025$) and the velocity perturbation appears at the third time step ($t = 0.050$).

Fig. 7 is the same as Fig. 6 but for the solutions of the second order accuracy. The velocity perturbation appears from the first step, $t = 0.025$. The amplitude of the perturbation is nearly the same as that in the solutions of the first order accuracy. As shown later, the perturbation can be suppressed if the initial state is slightly modified.

Fig. 8 shows the later stages of the solutions obtained with the first order Roe scheme. The top, middle and bottom panels show the density, the total pressure and the velocity, respectively. The colour denotes the epoch. The velocity perturbation observed in Fig. 6 evolves into sound waves propagating rightward and leftward of which phase velocity are $v_x + a = 2.342$ and $v_x - a = -0.225$ for the former and latter, respectively. In addition to the sound waves, the density profile has a dent around the contact discontinuity. The

Table 3. The initial state in the test problem of the advection of pressure balance mode.

	ρ	v_x	P_g	P_{cr}
Left ($x < 0$)	1.0	1.0	0.1	1.0
Right ($x \geq 0$)	1.0	1.0	1.0	0.1

dent grows in depth and in width. We need to suppress the sound waves of the numerical origin and growth of the dent.

This artificial wave excitation is due to the numerical diffusion of CR numbers. If we take account of numerical diffusion, equation (11) is rewritten as

$$\frac{\partial}{\partial t} \rho_{cr} + \nabla \cdot (\rho_{cr} \mathbf{v}) = \nabla \cdot (\eta \nabla \rho_{cr}), \quad (73)$$

where η denotes the effective diffusion coefficient. Hence equation (7) is rewritten as

$$\begin{aligned} \frac{\partial}{\partial t} (E_{cr}) + \nabla \cdot [(E_{cr} + P_{cr}) \mathbf{v} - \eta \nabla (E_{cr})] \\ = \mathbf{v} \cdot \nabla P_{cr} - \frac{\eta}{\gamma_{cr} P_{cr}} |\nabla P_{cr}|^2, \end{aligned} \quad (74)$$

where the second term in the right hand side denotes the net loss in the CR energy. Fig. 9 illustrates this mechanism of the loss in the CR energy

The loss in the CR energy is compensated by the gain in the gas energy, since the total energy is conserved. We can evaluate the change in the total pressure as follows. Given the CR pressure decrease by ΔP_{cr} , the CR energy decreases by

$$\Delta E_{cr} = \frac{\Delta P_{cr}}{\gamma_{cr} - 1}, \quad (75)$$

and the gas energy increases by the same amount. Hence the gas pressure increases by

$$\Delta P_g = -(\gamma_g - 1) \Delta E_{cr} = -\frac{\gamma_g - 1}{\gamma_{cr} - 1} \Delta P_{cr}. \quad (76)$$

Then the total pressure increases by

$$\Delta P_T = \frac{\gamma_{cr} - \gamma_g}{\gamma_{cr} - 1} \Delta P_{cr}, \quad (77)$$

since $\gamma_{cr} < \gamma_g$ and $\Delta P_{cr} < 0$.

The emission of the sound waves result in the decrease in the density. Thus, also the dent is due to the numerical diffusion of the CR pressure.

Although the numerical diffusion is inevitable, the effects can be alleviated by modifying the initial transition less sharp. If the initial profile is modified to be

$$q(x) = \frac{q_R + q_L}{2} + \frac{q_R - q_L}{2} \tanh\left(\frac{x}{h}\right), \quad (78)$$

where q and h denote a physical variable and the thickness of the transition layer, respectively. The subscripts, R and L, denote the values at the right and left states, respectively. Fig. 10 shows the effects of the modified initial profile. All the curves denote the solutions of the advection test at $t = 2.000$. The red and orange curves denote the solutions of which initial profile is given by equation (78) with $h = \Delta x = 0.1$. The red solution is obtained with the second order Roe scheme, while the orange is with the first order Roe scheme. The black and grey curves denote the

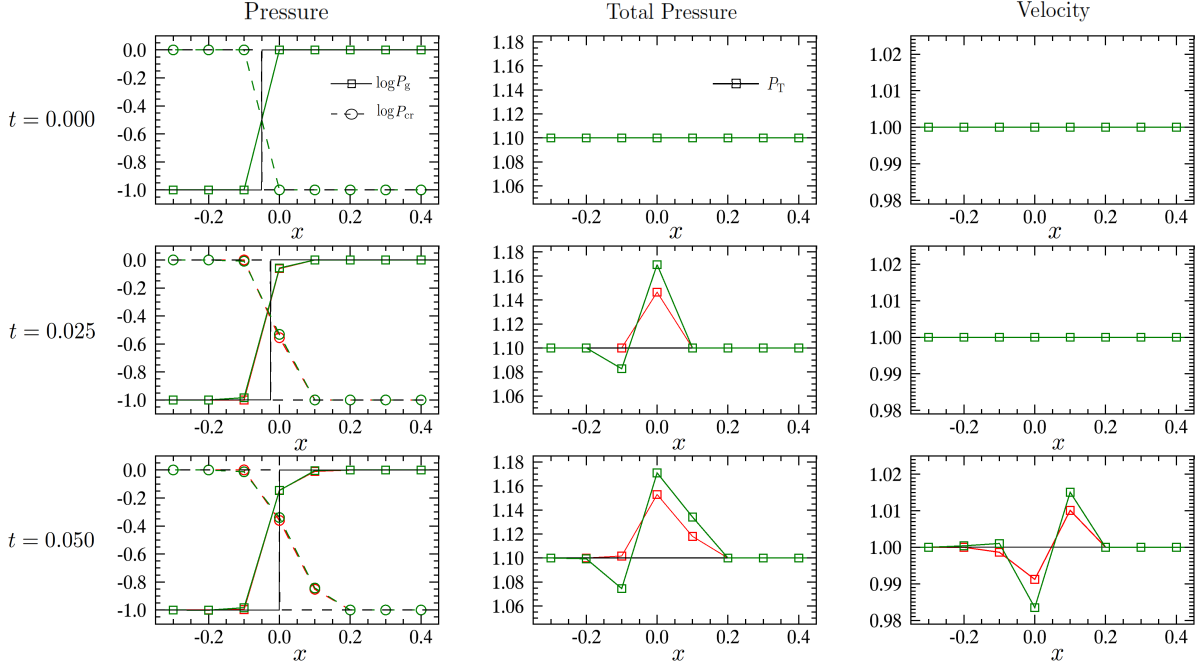


Figure 6. Test for the advection of the pressure balance mode. The top panels denote the gas pressure, the CR pressure, the total pressure, and the velocity in the initial state from left to right. The middle and bottom panels denote those at the first time step, $t = \Delta t$, and at the second time step, $t = 2\Delta t$, respectively. The green and red curves denote the solutions obtained with HLL and Roe-type numerical fluxes, respectively. The black line denotes the exact solution.

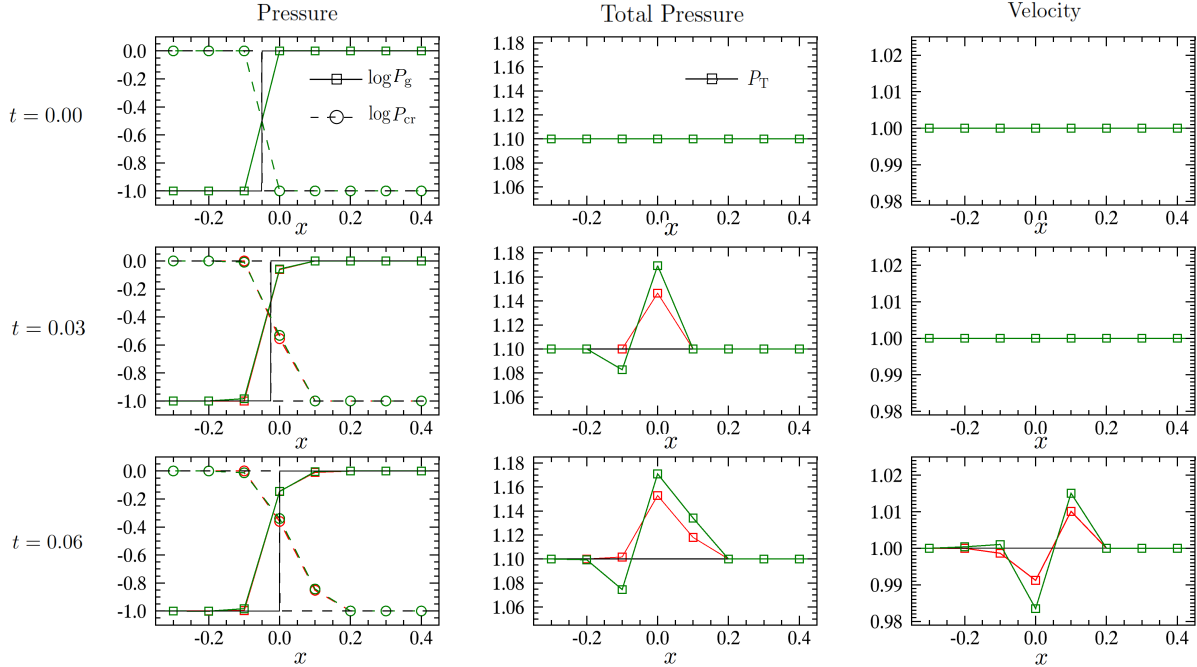


Figure 7. The same as Fig. 6 but for the 2nd order accuracy.

solutions of which initial state is denoted by a step function ($h = 0$). The black and grey solutions are obtained with the second and first order Roe schemes, respectively. Adoption of a second order scheme alone cannot suppress the numerical diffusion effectively. Only when $h \gtrsim \Delta x$, the numerical diffusion is suppressed sufficiently.

The Pdv scheme does not produce the spurious wave, since the source term vanishes in this test problem. The vdP scheme suffers from the spurious wave since the source term diverges at the front of the pressure balance mode. We have not tried to improve the vdP scheme to suppress the spurious

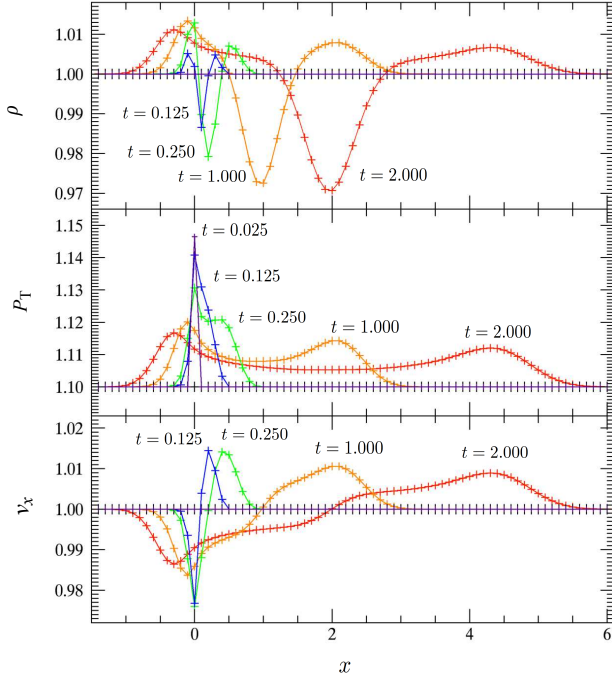


Figure 8. Late stages of the test problem shown in Fig. 6. The panels denote ρ , P_T , and v_x from the top to the bottom. The symbols and curves denote the solution at $t = 0.025, 0.125, 0.250, 1.0$, and 2.0 .

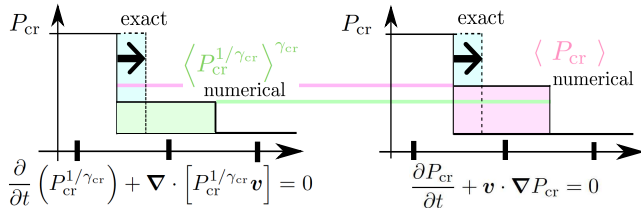


Figure 9. Illustration of the mechanism for the decrease in P_{cr} due to numerical diffusion by advection of the pressure balance mode. The left-hand panel denotes the numerical solution of the CR number conservation, while the right does that of the advection equation.

wave excitation, since the vdP scheme can not solve a shock wave properly.

We encounter a similar problem when solving the advection of the tangential shear. The shear velocity is smeared by numerical diffusion and hence a part of the kinetic energy is lost. The loss is compensated by the increase in the internal energy and hence the gas pressure increases spuriously around the shear. This problem is also alleviated by the same recipe.

3.4 1D MHD shock tube test

In this subsection we demonstrate that the 1D MHD shock tube problem can be solved with the Roe-type approximate Riemann solver. The initial state of the problem is summarized in Table 4. This problem is similar to the well-known one tested by Brio & Wu (1988). The resolution, the

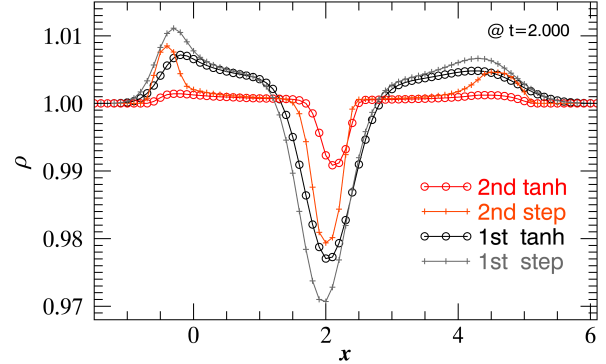


Figure 10. Compared are the numerical solutions of the advection test problem at $t = 2.0$. The initial state is expressed by equation (78) in the solutions denoted by red and black, while it is by the step function in the solutions denoted by orange and grey. The red and orange curves denote the solutions of the second order accuracy, while the black and grey do those of the first order accuracy. All the solutions are obtained with the Roe-type Riemann solver.

Table 4. Initial left- and right-state in the shock tube problem of modified Brio & Wu (1988).

	ρ	B_x	B_y	B_z	P_g	P_{cr}
Left ($x < 0$)	1.0	1.0	1.0	0.0	1.0	0.4
Right ($x \geq 0$)	0.125	1.0	-1.0	0.0	0.1	0.04

Table 5. Initial inside- and outside-state in the 2D MHD expansion.

	ρ	B_r	B_ϕ	B_z	P_g	P_{cr}
Inside	1.0	0.0	0.0	0.4472	2.0	1.0
Outside	0.2	0.0	0.0	0.4472	0.02	0.1

time step, and CFL number are taken to be $\Delta x = 1/256$, $\Delta t = 8 \times 10^{-4}$, and 0.843, respectively.

Fig. 11 shows the numerical solution at $t = 0.08$. The left-hand panels denote ρ , v_x , and ρv_x , respectively. The solid curves with the open squares denote the numerical solution while the dashed ones do the initial state. The top central panel denotes P_T (red), P_g (purple), and P_{cr} (yellow green), while the middle central one does v_y (brown) and B_y (black), and the bottom central one does ρv_y . The right-hand panels denote s , χ , and $E + E_{cr}$, respectively.

The solution shows the fast rarefaction wave, the slow shock, the contact discontinuity (the pressure balance mode), the slow compound, and the fast rarefaction, from right to left. Note that the contact discontinuity and the pressure balance mode are solved sharply. The CR concentration, χ , changes only at the contact discontinuity.

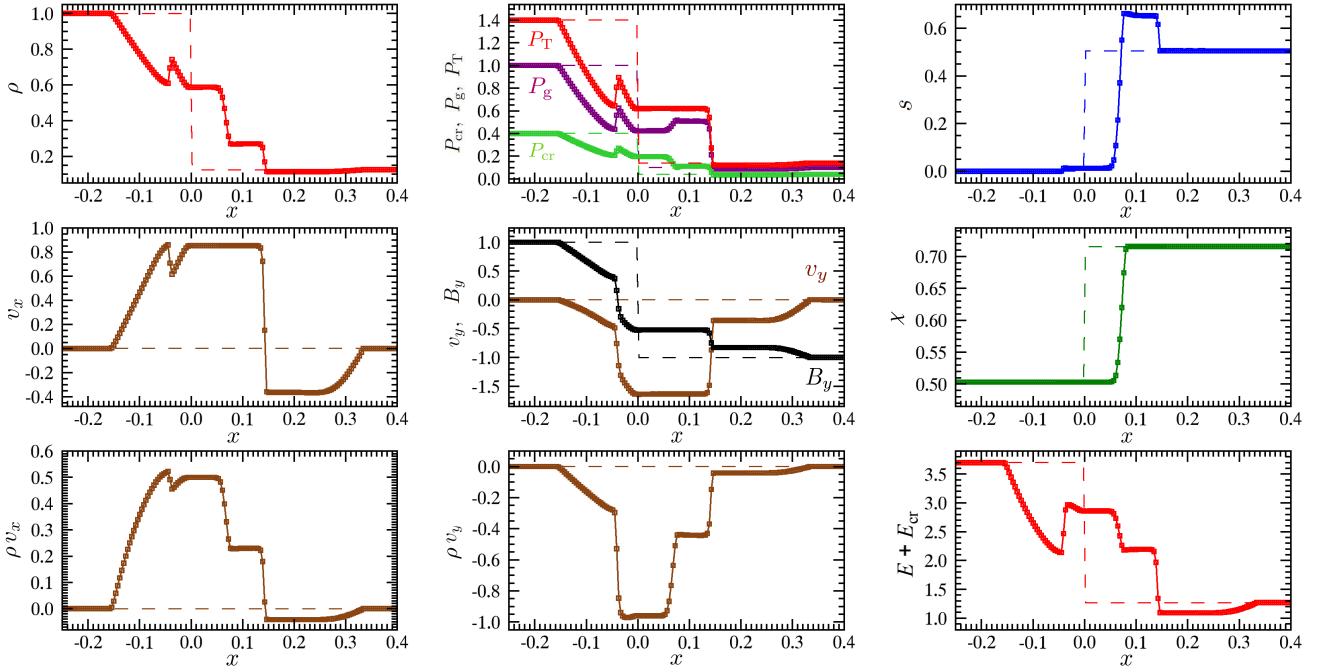


Figure 11. An example of CR MHD shock tube problem. Top: the density, CR pressure, gas pressure, total pressure, and entropy from left to right. Middle: the velocity, magnetic field, and CR concentration from left to right. Bottom: the x - and y -components of the momentum density, and the total energy density from left to right.

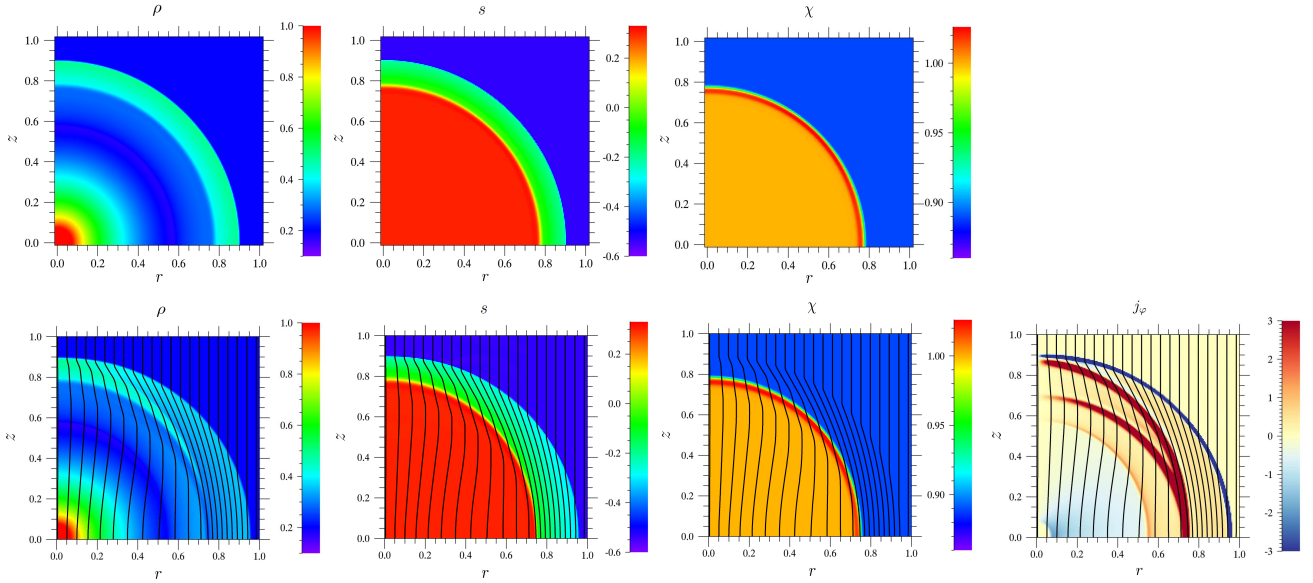


Figure 12. Expansion of a high pressure sphere. Top: the density, entropy, and CR concentration in HD expansion problem from left to right. Bottom: the density, entropy, CR concentration, and electric current density in MHD problem. The initial states are the same except for the initial magnetic field. The black curves denote the magnetic field in the bottom panels.

3.5 2D MHD expansion

In this subsection we consider an expansion of a hot sphere. We use the cylindrical coordinates, (r, φ, z) , and assume the symmetry around the z -axis. The gas pressure is higher inside the sphere of $\sqrt{r^2 + z^2} = 0.5$ in the initial state. It is

assumed to have the profile,

$$P_g(r, z) = P_{g,\text{in}} + \frac{(P_{g,\text{out}} - P_{g,\text{in}})}{2} \times \left[\tanh \left(\frac{\sqrt{r^2 + z^2} - 0.5}{0.01} \right) + 1 \right], \quad (79)$$

where the subscripts, in and out, denote the values inside and outside the sphere, $\sqrt{r^2 + z^2} = 0.5$. Also the CR pres-

sure and density are assumed to have similar profiles. The parameters are summarized in Table 5. The velocity is assumed to vanish in the initial state. The spatial resolution, time step, and CFL number are taken to be $\Delta x = \Delta z = 1/200$, $\Delta t = 5 \times 10^{-4}$, and 0.340 respectively.

We construct two models having the same initial ρ , P_g , and P_{cr} . The magnetic field vanishes in the first model while it is uniform and has only the z -component in the second model. The plasma beta is $\beta = 20$ inside and 2 outside the sphere in the second model. We solved this model with the Roe-type approximate Riemann solver.

Fig. 12 denotes the stage at $t = 0.19$. The top panels denote ρ , s , and χ in the first model from left to right. The values are shown by colour and the colour bars are shown in the right of each panel. They show spherical shock wave propagating outward and rarefaction propagating inward. The contact discontinuity and pressure balance mode are clearly resolved.

The bottom panels denote ρ , s , χ , and the electric current density, j_φ . The colour denotes the values while the black contours do the magnetic field lines. The expansion is aspherical due to the magnetic field. The model shows three shock waves: a fast shock wave and two slow shock waves. The magnetic field is bent sharply at the shock fronts. Note that the electric current density is confined at the shock fronts and in the rarefaction wave. This example demonstrates that the multi-dimensional CR MHD equations can be solved successfully if we employ the fully conservation form.

4 DISCUSSIONS AND CONCLUSIONS

We have succeeded in rewriting the CR MHD equations in the fully conservation form as shown in Section 2. We discuss the advantages of the fully conservation form in this section.

First the Rankine-Hugoniot relation is automatically fulfilled when the CR MHD equations are integrated in the fully conservation form. Thus, the jumps in the density and pressure at MHD shocks are evaluated correctly in the solutions. When we integrate the CR MHD equations in the original form, the numerical solution may violate the Rankine-Hugoniot relation as shown in Section 3.3.

One might think that any shock tube problems could be solved without using the fully conservation form. Dubois & Commerçon (2016) have succeeded in solving a CR shock tube problem posed by Pfrommer et al. (2006) by evaluating Pdv as the source term. However, the success is in part due to the fact that CR pressure is smaller than the gas pressure in the post-shocked gas. Table 7 summarizes the pressure and density distributions in the test problem. The number in the first column species the intervals where the density and pressure are constant in the Riemann solution (see Fig. 2). The values in regions 2 and 3 are given by the Riemann solution and match their Fig. 3. The CR pressure is dominant in regions 3 and 5 while it is not in region 2, i.e., in the post-shocked gas. Then the source term has a minor contribution at the shock front. See Appendix B for more details on these test problems.

Pfrommer et al. (2006) also succeeded in solving a shock tube problem with their smoothed particle hydrodynamics (SPH) code, although their solution shows small oscillations

Table 6. The shock tube problem of Dubois & Commerçon (2016). The adiabatic indexes are taken to be $\gamma_g = \gamma_{cr} = 1.4$ in this test problem.

Region	ρ	P_g	P_{cr}
1	0.100	0.066	0.034
2	0.204	0.192	0.093
3	0.408	0.097	0.187
5	1.000	0.340	0.660

Table 7. The shock tube problem of Pfrommer et al. (2006).

Region	ρ	$P_g (\times 10^4)$	$P_{cr} (\times 10^4)$
1	0.200	0.024	0.024
2	0.796	5.141	0.147
3	0.400	1.455	3.832
5	1.000	6.700	13.000

around shock front and contact discontinuity. However, the CR pressure is much smaller than the gas pressure in the post-shocked gas. Table 7 is the same as Table 6 but for the shock tube problem shown in Fig. 1 of Pfrommer et al. (2006).

The violation of the Rankine-Hugoniot relation is serious when the CR pressure dominates in the post-shocked gas. A clear example is shown in Section 3.3.

The fully conservation form has another advantage, adaptation to higher order scheme. Various standard higher order schemes are available, when differential equations are written in the fully conservation form. see e.g. Toro 2009 for the methods to achieve higher order accuracy. Remember that the source terms and numerical fluxes have been evaluated separately. Thus the source term can be another source of numerical oscillation when it is evaluated to be of higher order accuracy in space.

The fully conservation form may be useful when we take account of injection of CRs. CRs can be generated from supernova explosions and diffusive shock acceleration. The generation can be taken into account in the CR MHD equations, if it is modelled successfully (see e.g. Zank et al. 1993; Jubelgas et al. 2008; Vazza et al. 2012). Thus far, only the energy injection rate, is taken into account in the literature. However, we can take account of both the energy injection rate, S_E , and the injection rate in number, S_ρ , in the fully conservation form. In the following we assume that E_{cr} and ρ_{cr} are related by

$$E_{cr} = \frac{K \rho_{cr}^{\gamma_{cr}}}{\gamma_{cr} - 1}, \quad (80)$$

where K denotes the CR *entropy* and has been assumed to be $K = 1$ thus far. If the injection is taken into account, the change in K should be described as

$$\frac{1}{K} \frac{dK}{dt} = \frac{S_E}{E_{cr}} - \gamma_{cr} \frac{S_\rho}{\rho_{cr}} \quad (81)$$

$$= \frac{S_\rho}{E_{cr}} \left(\frac{S_E}{S_\rho} - \gamma_{cr} \frac{E_{cr}}{\rho_{cr}} \right), \quad (82)$$

where dK/dt denotes the Lagrangian derivative. Equation

(82) follows the change the average energy of CRs, $E_{\text{cr}}/\rho_{\text{cr}}$. The average CR energy is important information to estimate the diffusion coefficient.

This paper has proved the usefulness of CR number conservation, equation (11). It is derived from and equivalent to the CR energy equation, equation (7). However, the former is written in the fully conserved form, while the latter is not. The former is more suitable for numerical analysis than the latter, since the approximate Riemann solutions are given explicitly and hence shock waves are reproduced without numerical oscillations. The derived approximate Riemann solutions are only slightly different from those for the ideal MHD equations: the sound speed is modified by inclusion of the CR pressure and a new mode, the pressure balance mode, is added. Thus we can construct higher order scheme by applying the methods developed for the ideal MHD equations. We have also suggested to extend the CR MHD equations by introducing the CR entropy. This extension enables us to evaluate the average CR energy. It should be useful to estimate the diffusion and emission from CRs.

ACKNOWLEDGEMENTS

We thank Ryoji Matsumoto and Yosuke Matsumoto for their helpful discussions and suggestions.

REFERENCES

- Berezinskii V. S., Bulanov S. V., Dogiel V. A., Ptuskin V. S., 1990, *Astrophysics of cosmic rays*
 Brio M., Wu C. C., 1988, *Journal of Computational Physics*, 75, 400
 Bykov A. M., 2014, *A&ARv*, 22, 77
 Dubois Y., Commerçon B., 2016, *A&A*, 585, A138
 Fahr H. J., Kausch T., Scherer H., 2000, *A&A*, 357, 268
 Florinski V., Ferreira S. E. S., Pogorelov N. V., 2013, *Space Sci. Rev.*, 176, 147
 Hanasz M., Lesch H., 2003, *A&A*, 412, 331
 Hanasz M., Lesch H., Naab T., Gawryszczak A., Kowalik K., Włotański D., 2013, *ApJ*, 777, L38
 Jubelgas M., Springel V., Enßlin T., Pfrommer C., 2008, *A&A*, 481, 33
 Kudoh Y., Hanawa T., 2016, *Journal of Physics Conference Series*, 719, 012021
 Kuwabara T., Nakamura K., Ko C. M., 2004, *ApJ*, 607, 828
 Longair M., 1994, *High Energy Astrophysics: Volume 2, Stars, the Galaxy and the Interstellar Medium*. Cambridge University Press
 Parker E. N., 1966, *ApJ*, 145, 811
 Parker E. N., 1967, *ApJ*, 149, 535
 Pfrommer C., Springel V., Enßlin T. A., Jubelgas M., 2006, *MNRAS*, 367, 113
 Potgieter M., 2013, *Living Reviews in Solar Physics*, 10
 Rasera Y., Chandran B., 2008, *ApJ*, 685, 105
 Roe P. L., 1981, *Journal of Computational Physics*, 43, 357
 Ryu D., Jones T. W., 1995, *ApJ*, 442, 228
 Salem M., Bryan G. L., 2014, *MNRAS*, 437, 3312
 Tielens A., 2010, *The Physics and Chemistry of the Interstellar Medium*. Cambridge University Press
 Toro E., 2009, *Riemann Solvers and Numerical Methods for Fluid Dynamics: A Practical Introduction*. Springer Berlin Heidelberg
 Vazza F., Brüggemann M., Gheller C., Brunetti G., 2012, *MNRAS*, 421, 3375

- Vazza F., Ferrari C., Brüggemann M., Bonafede A., Gheller C., Wang P., 2015, *A&A*, 580, A119
 Webb G. M., Brio M., Zank G. P., Story T., 1995, *ApJ*, 442, 822
 Yang H.-Y. K., Ruszkowski M., Ricker P. M., Zweibel E., Lee D., 2012, *ApJ*, 761, 185
 Zank G. P., Webb G. M., Donohue D. J., 1993, *ApJ*, 406, 67
 Zweibel E. G., 2013, *Physics of Plasmas*, 20, 055501
 van Leer B., 1979, *Journal of Computational Physics*, 32, 101

APPENDIX A: ROE-TYPE APPROXIMATE RIEMANN SOLVER

In this appendix we derive the Roe-type approximate Riemann solver for the CR HD equations from equations (37) through (42). They show that the spatial difference is decomposed into four waves. When the wave speeds (λ_i) and eigenvectors (\mathbf{r}_i) are evaluated by the Roe-average defined as

$$\begin{aligned}\bar{\rho} &= \sqrt{\rho_{j+1}\rho_j}, \quad \bar{v}_x = \frac{\sqrt{\rho_{j+1}}v_{x,j+1} + \sqrt{\rho_j}v_{x,j}}{\sqrt{\rho_{j+1}} + \sqrt{\rho_j}}, \\ \bar{H} &= \frac{\sqrt{\rho_{j+1}}H_{j+1} + \sqrt{\rho_j}H_j}{\sqrt{\rho_{j+1}} + \sqrt{\rho_j}}, \\ \bar{P}_T &= \frac{\sqrt{\rho_{j+1}}P_{T,j} + \sqrt{\rho_j}P_{T,j+1}}{\sqrt{\rho_{j+1}} + \sqrt{\rho_j}}, \\ \bar{\rho}_{\text{cr}} &= \frac{\sqrt{\rho_{j+1}}\rho_{\text{cr},j} + \sqrt{\rho_j}\rho_{\text{cr},j+1}}{\sqrt{\rho_{j+1}} + \sqrt{\rho_j}}, \\ \bar{a}^2 &= (\gamma_g - 1) \left(\bar{H} - \frac{\bar{v}_x^2}{2} - \frac{\bar{\rho}_{\text{cr}}}{\bar{\rho}} \zeta \right), \\ \zeta &= \frac{\gamma_g - \gamma_{\text{cr}}}{(\gamma_g - 1)(\gamma_{\text{cr}} - 1)} \frac{P_{\text{cr},j+1} - P_{\text{cr},j}}{\rho_{\text{cr},j+1} - \rho_{\text{cr},j}}.\end{aligned}\tag{A1}$$

the spatial difference is decomposed into the linear combination at the waves completely (see e.g. Toro 2009). Here the subscripts, j and $j+1$, specify the cells at the centre of which the variables are evaluated.

The Roe-type numerical flux is given by

$$\mathbf{F}_{j+1/2}^{\text{Roe}} = \frac{1}{2} \left(\mathbf{F}_{j+1} + \mathbf{F}_j - \sum_i w_i |\lambda_i| \mathbf{r}_i \right),\tag{A2}$$

where the subscript $j+1/2$ denotes the value on the surface between the j -th and $j+1$ -th cells.

The Roe-type numerical flux is obtained similarly for the CR MHD equations. The Roe-averaged magnetic field is given by

$$\bar{B}_y = \frac{\sqrt{\rho_j}B_{y,j+1} + \sqrt{\rho_{j+1}}B_{y,j}}{\sqrt{\rho_{j+1}} + \sqrt{\rho_j}},\tag{A3}$$

$$\bar{B}_z = \frac{\sqrt{\rho_j}B_{z,j+1} + \sqrt{\rho_{j+1}}B_{z,j}}{\sqrt{\rho_{j+1}} + \sqrt{\rho_j}}.\tag{A4}$$

APPENDIX B: SHOCK TUBE PROBLEMS

We reexamine the shock tube problems examined in earlier works.

Fig. A1 shows the solutions of the shock tube problem of Dubois & Commerçon (2016) of which initial state is summarized in Table 6. We have solved the problem on

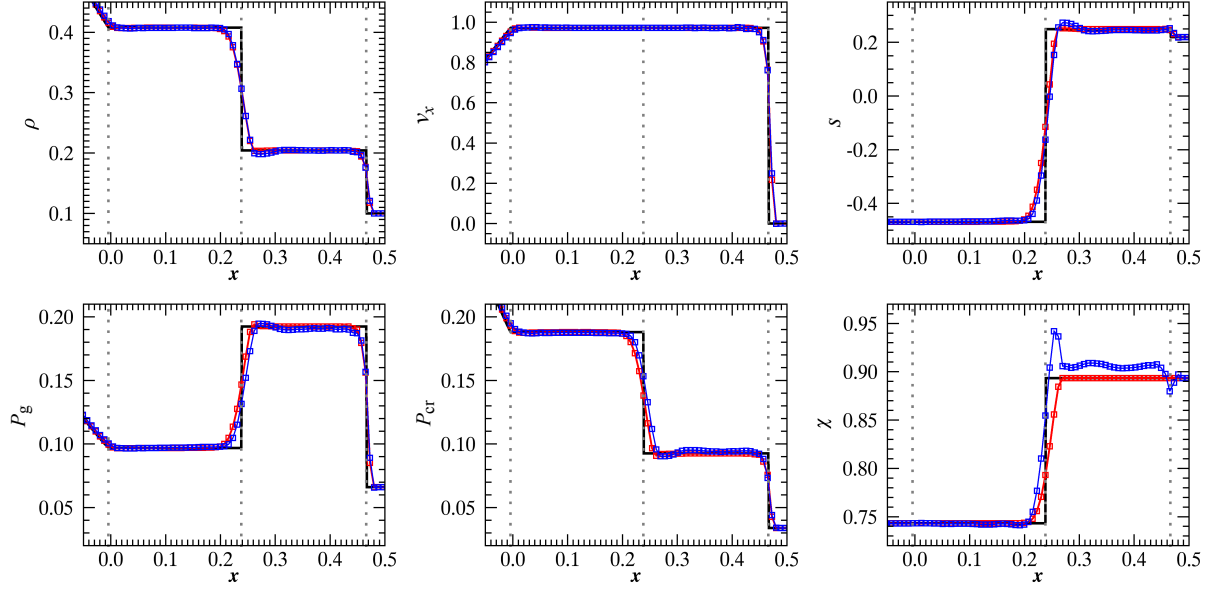


Figure A1. The CRHD shock tube problem of Dubois & Commerçon (2016). The grey dotted lines denote the tail of rarefaction ($x = 4.218 \times 10^{-3}$), contact discontinuity ($x = 0.2380$), and shock ($x = 0.4660$) at $t = 0.245$ from left to right. The CFL number is taken to be 0.743.

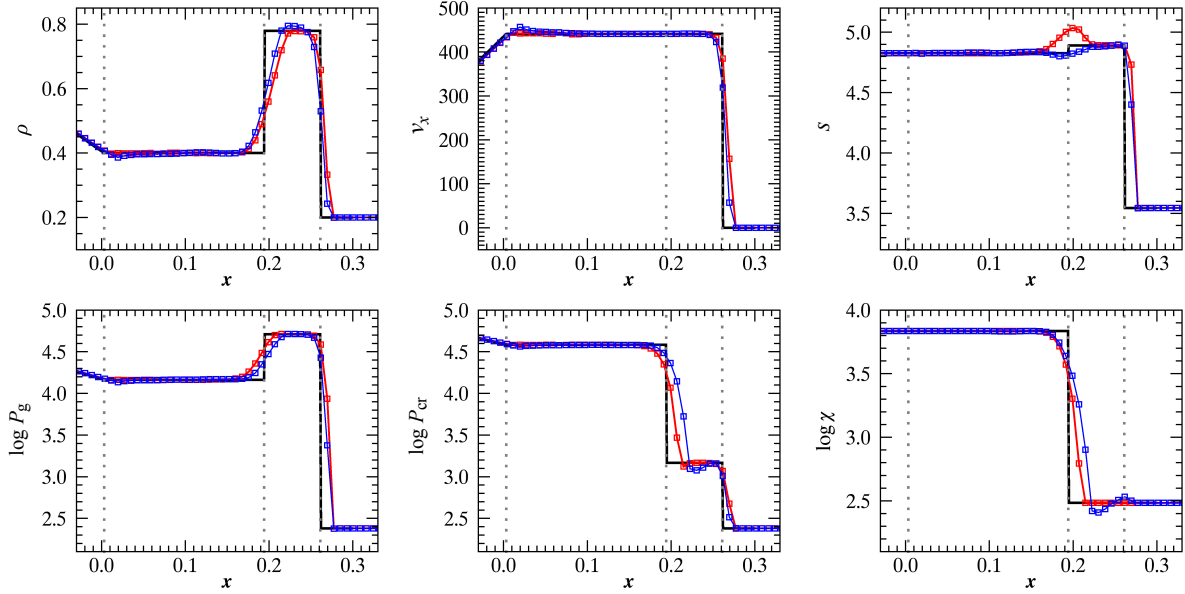


Figure A2. The CRHD shock tube problem of Pfrommer et al. (2006). The grey dotted lines denote the tail of rarefaction ($x = 3.232 \times 10^{-3}$), contact discontinuity ($x = 0.1942$), and the shock ($x = 0.2612$) at $t = 4.4 \times 10^{-4}$ from left to right. The CFL number is taken to be 0.794.

the uniform cell width of $\Delta x = 1/128$ with the time step, $\Delta t = 2.45 \times 10^{-3}$. The blue and red curves denote the solutions at $t = 0.245$ obtained with Pdv scheme and ours, respectively. The exact solution is denoted by the black. The upper panels denote ρ , v_x and s as a function of x from left to right, while the lower panels do P_g , P_{cr} , and χ . Only the region of $-0.05 \leq x \leq 0.50$ is shown. The Pdv scheme gives an apparently good approximation for ρ , v_x , s , P_g , and P_{cr} but not for χ . Our scheme provides a better approximation.

The spurious sound wave emission is not observed in this test problem since $\gamma_g = \gamma_{cr} = 1.4$. This is because the spurious increase in the pressure is proportional to $\gamma_g - \gamma_{cr}$ as shown in equation (77).

Fig. A2 shows the solutions of the shock tube problem Pfrommer et al. (2006) of which initial state is given in Table 7. Also this problem has been solved on the uniform cell width of $\Delta x = 1/128$ with the time step, $\Delta t = 8.0 \times 10^{-6}$. The solution at $t = 4.4 \times 10^{-4}$ obtained with the Pdv scheme

is denoted by the blue curves, while that obtained with our scheme is by the red ones. The black curves denote the exact solution. Each panel shows ρ , v_x , s , $\log P_g$, $\log P_{cr}$, and $\log \chi$. In this example, both the schemes provide a good approximation. This is mainly because the CR pressure is by a factor of 10 lower than the gas pressure between the contact discontinuity and the shock front ($0.1942 \leq x \leq 0.2612$).

This paper has been typeset from a $\text{\TeX}/\text{\LaTeX}$ file prepared by the author.